ACS OMEGA

http://pubs.acs.org/journal/acsodf

Article

Optimal Operation of an Oscillatory Flow Crystallizer: Coupling Disturbance and Stability

Shi-jun Lian, Zhong-xin Hu, Zhong Lan,* Rong-fu Wen, and Xue-hu Ma

Cite This: *ACS Omega* 2021, 6, 28912−28922

Read Online

ACCESS | Metrics & More | Article Recommendations

ABSTRACT: In the process of industrial crystallization, it is always difficult to balance the secondary nucleation rate and metastable zone width (MSZW). Herein, we report an experimental and numerical study for the cooling crystallization of paracetamol in an oscillatory flow crystallizer (OFC), finding the optimal operating conditions for balancing the secondary nucleation rate and MSZW. The results show that the MSZW decreases with the increase of oscillation Reynolds number (Re_o). Compared to the traditional stirring system, the OFC has an MSZW three times larger than that of the stirring system under a similar power density of consumption. With the numerical simulation, the OFC can produce a stable space environment and instantaneous strong disturbance, which is conducive to the crystallization process. Above all, a high Re_o is favorable to produce a sufficient nucleation rate, which may inevitably constrict the MSZW to a certain degree. Then, the optimization strategy of the operating parameter (Re_o) in the OFC is proposed.

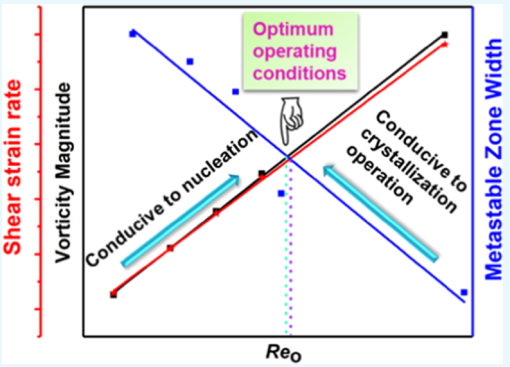

1. INTRODUCTION

Crystallization is a common and significant phase transition process that has been widely used in various fields, such as petroleum chemistry, pharmaceutical industry, fine chemicals, and even semiconductor materials.[1−6] Consideing the pharmaceutical industry as an example, nearly 90% of the active pharmaceutical ingredients (APIs) are presented as organic crystals.[7] To fulfill the ever-growing demand for crystal products, it is particularly important to deeply study the details and precise control of the crystallization process for the improvement of the crystal quality, which is determined by its purity, size, and morphology.[8,9] The crystallization process includes nucleation and growth, in which nucleation is divided into primary nucleation and secondary nucleation. The secondary nucleation always accompanies the primary nucleation, and moreover, the former is apt to be the predominant mechanism of nucleation.[10] The common industrial crystallization process is a typical secondary nucleation process, which needs to add a certain number of seeds. The seeds provide surface areas for growth and the source of crystals to enable secondary nuclei under suitable conditions.

Thus, to control the nucleation and crystal growth, it is first necessary to establish a relatively wide operation window (metastable zone) to improve the crystallizing efficiency under relatively high supersaturation, requiring a mild and uniform crystallization system. Otherwise, the crystallization system needs a certain disturbance (e.g., fluid shear, fluid mixing) to complete the secondary nucleation requirements. Simultaneously, this disturbance cannot stay at a fixed position for a long time, which will affect the quality of the crystals (e.g., particle size distribution, crystal polymorphs).[11] During the traditional crystallization process, the disturbance can be provided by the fluid mixing caused by the impeller. However, the stirred tank always fails to provide an entirely uniform crystallization environment even with the optimum mixing characteristics; this is typical because turbulence intensity is extremely variable in a stirred tank and this is exacerbated as the scale of the system increases.[12] In particular, the shear stress distribution and turbulent intensity near the impeller will induce the earlier occurrences of nucleation in the crystallization process, which will generate smaller sizes of crystals due to excessive secondary nucleation.[8,12−14]

To avoid the disadvantage of the stirring system which has been mentioned above, the local disturbance should be distributed periodically in the internal space of the crystallizer. Therefore, the development of a comprehensive technique that can provide both sufficient metastable zone width (MSZW) and appropriate flow disturbance for secondary nucleation is imperative for improving the quality of industrial crystalliza-

Received: July 21, 2021
Accepted: October 13, 2021
Published: October 24, 2021

tion. Accordingly, an oscillatory flow crystallizer (OFC) has been considered to be a promising candidate to avoid mechanical agitation effects,[15−23] as it can generate recirculation flow and vortex through the combination of a reactor structure and oscillation process.[24] This unique flow can create a series of well-mixed volumes, which is beneficial to control mass and heat transfer.[25−28] Furthermore, the appropriate residence time in the OFC can also improve the quality of the crystals produced. It is certain that the employment of the OFC for crystallization can reach the requirement of flow field mixing; however, the principle on how to balance the relationship between the stable environment and appropriate disturbance has rarely been reported. Although many efforts have been made to study the performance of the OFC based on operating parameter control related to the product quality indicators,[29−33] the mechanism on how crystal generation is affected by flow characteristics is still unclear.

Herein, we focus on finding the balance between a relatively wide metastable zone and appropriate secondary nucleation rate through controlling the oscillatory flow according to the flow characteristics on the OFC. The aim of this work is to provide a basis for the optimization design and operation of the industrial crystallization process. The specific research contents are as follows:

- First, according to the smooth periodic constrictions of the OFC, the influence and advantages of oscillatory flow on controlling the metastable zone have been investigated through experiments and literature comparison to verify the possibility of a wider operation window in the OFC.
- Second, the response and evolution of the flow field in the OFC have been analyzed to prove that the flow field can satisfy the stability and local disturbance of the crystallization system at the same time, which are conducive to crystal nucleus growth and secondary nucleation, respectively.
- Finally, based on the balance mechanism between the intensity of flow field disturbance and the MSZW, we propose a strategy to find the optimal operating parameter Reynolds number (Re_o) in the OFC.

2. EXPERIMENTAL SECTION

This section outlines the details of the crystallization experiments performed for the measurements of the MSZW. The cooling crystallization process of the paracetamol−water solution is chosen as the experimental model. Paracetamol is supplied by Aladdin, with a purity of 99.9%. The water is deionized water.

2.1. Experimental Setup and Procedure. Figure 1 shows the experimental system (left) and the size of the OFC (right). The experimental system consists of three parts: a cooling circulation system, an oscillation generation system, and an optical detection system. The crystallizer is made of quartz glass for optical detection with a total length of 260 mm, in which an inner tube is a smooth periodic constriction structure with an inner diameter of 10 mm and a necking diameter of 5 mm. The outer tube jacket is water-cooled. The oscillation frequency is provided by a digital controlling motor, which is set to 1.4, 1.9, 2.3, 2.7, and 4.3 Hz, depending on the experiment, with a constant amplitude of 0.0115 m. The corresponding range of Re_o is 914−2808. The circulating water is cooled by a temperature control device (supplied by Julabo),

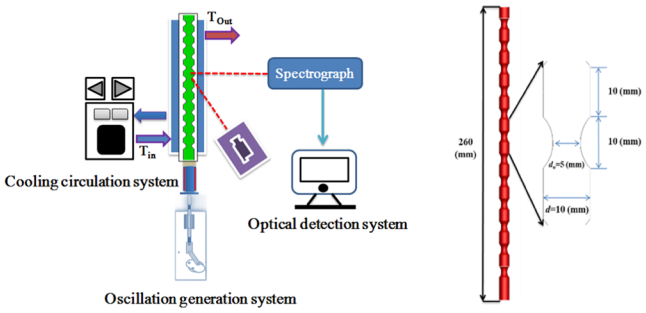

Figure 1. Schematic diagram showing the experimental setup (left) and dimensions (right) of the OFC.

and spontaneous nucleation is detected by a spectrometer (supplied by Ocean Optics), whose working principle is detailed in Section 2.2.

According to the solubility curve equation of the paracetamol−water solution regressed by Cruz et al.,[34] the saturated solutions at different temperatures are prepared in Table 1. The solution is then added to the preheated (10 °C above saturation temperature) OFC to ensure no nucleation. To remove air bubbles in the OFC, the solution is oscillated at a high frequency for 5 min and then reduced to the required frequency for the experiment. The circulating water in the jacket is cooled at a specific cooling rate (5, 10, 15, 20, 25, and 30 °C·h^{-1}), while the spontaneous nucleation is detected by the spectrometer. To ensure the accuracy of the experimental results, each group of experiments is repeated twice.

Table 1. Initial Saturation Temperature and Concentration

	T^*(°C)	C^*(g·kg^{-1})
1	30	17.2
2	35	19.9
3	40	23.1
4	45	26.7

The following two dimensionless formulas for characterizing the oscillatory flow devices are introduced[35−37]

$$Re_o = \frac{2\pi f x_0 d\rho}{\mu} \quad (1)$$

$$St = \frac{d}{4\pi x_o} \quad (2)$$

where Re_o denotes the so-called oscillation Reynolds number, which indicates the mixing intensity in the crystallizer. The Strouhal number (St) indicates the propagation degree of eddies, where d is the diameter of the tube, ρ is the density of the solution, f is the oscillation frequency, x_o is the amplitude, and μ is the viscosity of the solution.

For the OFC system, the power density, P/V (w·m^{-3}), represents the input power per unit volume in the system, which is usually used for "equivalents" comparison with a stirred tank reactor (STR).[8] It can be calculated by the revised quasi-steady-flow model, which is proposed by Jimeno et al. for the smooth-edged-baffles of an oscillatory flow reactor, as shown below[38]

$$\frac{P}{V} = \frac{2{n_o}^{0.7}\rho}{3\pi C_D^2 (V/A)}\left(\frac{1-\alpha^2}{\alpha^2}\right)x_o^3(2\pi f)^3 \quad (3)$$

https://doi.org/10.1021/acsomega.1c03890
ACS Omega 2021, 6, 28912−28922

where n_o is the number of orifices, C_D is the coefficient of discharge of the baffles (0.8), V is the volume of the reactor, A is the cross-sectional area of the reactor, and α is the baffle-free area ratio ($\alpha = (d_o/d)^2$).

2.2. Spontaneous Nucleation Detection. Since no complete theory is available to model the nucleation and crystallization processes, they can only be anticipated through experimentation; accurate experimental measurements are essential for understanding crystallization processes.[39] A number of detection methods are used for the metastable zone in the crystallization process, such as turbidity,[39−42] attenuated total reflection Fourier transform infrared (ATR-FTIR) spectroscopy,[43−46] focused beam reflectance measurements (FBRMs),[44,46−48] and particle vision and measurement (PVM).[47] Most of the methods require a probe to be placed within the crystallizer, which can affect the crystallization process more or less.[49] In this study, the laser scattering system performs as a noninvasive detection and avoids the above effects. The principle of detection that responds to the nucleation occurrence is laser Mie scattering. When a 632 nm laser passes through the solution, the Mie scattering intensity is detected by a spectrometer (supplied by Ocean Optics) in the vertical direction. The sampling frequency can reach 10 Hz, and the spontaneous nucleation is characterized by the sudden enhancement of the scattering intensity. At the same time, the temperature of the cooling system and the solution is recorded by the data collector. Therefore, the MSZW can be calculated by the difference between the saturated temperature of the solution and the temperature at which the crystals are detected.

As shown in Figure 2, the typical curves of the scattering intensity and the solution temperature under the specified

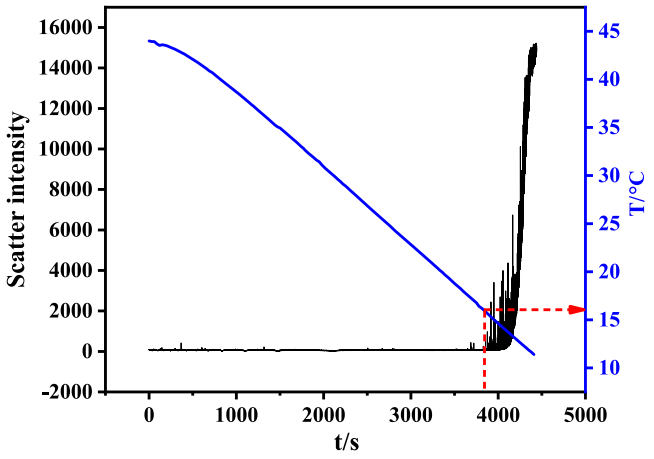

Figure 2. Detection of nucleation by laser scattering.

solution concentration and the cooling rate are illustrated. Here, the turning point of the red dotted line is the time of nucleation and the corresponding solution temperature.

2.3. Theory of Nucleation Kinetics and Experimental Data Processing. According to Nyvlt's classic theory of nucleation kinetics,[50] the primary nucleation rate, J_n, can be written as the following power-law function of supersaturation

$$J_n = k_n' \Delta C^n a \tag{4}$$

where k_n is the number of nucleation rate constant and n is the nucleation order. ΔC is the supersaturation ($\Delta C = C - C^*$), where C is the concentration and C^* is the solubility concentration. For the cooling crystallization, the rate of the supersaturation generation can be expressed as a function of the cooling rate ($\beta = (-dT)/dt$) as follows

$$\frac{d\Delta C}{dt} = \beta\left(\frac{dc^*}{dT}\right) \tag{5}$$

where $(dc^*)/dT$ is the slope of the solubility curve for a given saturation temperature. The maximum supercooling ($\Delta T_{max} = T^* - T_{nuc}$, where T^* is the solubility temperature and T_{nuc} is the temperature corresponding to the spontaneous nucleation) is related to the maximum supersaturation (ΔC_{max}) as follows

$$\Delta C_{max} = \frac{dc^*}{dT}\Delta T_{max} \tag{6}$$

Basically, while the system achieves the supersaturation through moderate cooling, the nucleation rate at the beginning of nucleation is equal to the supersaturation rate in a certain period. The growth rate of the initial nucleation is ignored during this period.[50] Therefore, the mass and number of nuclei formed can be written as follows

$$J_m = k_n' h \rho_p r^3 \Delta C^n = k_n \Delta C^n \tag{7}$$

where J_m is the mass nucleation rate and k_n is the mass nucleation rate constant. Also, h is the volume shape factor, ρ_p is the density of the solute crystals, and r is the nucleus size.

Combining eqs 5−7, the following is obtained

$$k_n \Delta C^n = k_n\left[\frac{dc^*}{dT}\Delta T_{max}\right]^n = \beta\left(\frac{dc^*}{dT}\right)\varepsilon \tag{8}$$

where ε is a conversion factor ($\varepsilon = 1$).[41]

Taking the logarithm on both sides of eq 8, we get the following expression

$$\ln(\beta) = (n-1)\ln\left(\frac{dC^*}{dT}\right) + \ln(k_n) + n\ln(\Delta T_{max}) \tag{9}$$

A straight line can be fitted by plotting $\ln(\beta)$ and $\ln(\Delta T_{max})$, in which the slope is the nucleation order n and the mass nucleation rate constant k_n can be obtained with the intercept.

3. NUMERICAL SIMULATIONS

3.1. Model Equations. Based on the continuous crystallization process, the details of fluid flow in the OFC are investigated by numerical simulation. The nucleation and growth of crystals are not considered in the simulation process, and no particle−particle interaction or particle diffusion in the liquid phase are included in the model. The simulations are performed in FLUENT 19.0 using the finite volume method. A three-dimensional numerical model is established, which is consistent with the size of the experimental equipment. All simulations are performed using a laminar solver; this is consistent with the literature because the solver has been widely used in the past,[51−54] even if the Re_o value is as high as 8043.[27,55] The set of standard incompressible mass-conservation, Navier−Stokes, and energy equations (eqs 10−12) are considered.

$$\frac{\partial \rho}{\partial t} + \nabla \times (\rho v) = 0 \tag{10}$$

$$\rho\left(\frac{\partial v}{\partial t} + v \times \nabla v\right) = \rho g - \nabla P + \mu \nabla^2 v \tag{11}$$

https://doi.org/10.1021/acsomega.1c03890
ACS Omega 2021, 6, 28912−28922

$$\frac{\partial(\rho T)}{\partial t} + \nabla \times (\rho v T) = \nabla \times \left(\frac{k}{C_P}\mathrm{grad}(T)\right) + S_T \quad (12)$$

where v is the velocity, P is the pressure, μ is the viscosity, C_p is the specific heat, k is the thermal conductivity, and T is the temperature.

Since the common industrial crystallization process is a typical secondary nucleation process, the influence of crystal particles on the flow field needs to be considered. The trajectory of each discrete particle is predicted by integrating the force balance on the particle as follows

$$m_p \frac{dv_p}{dt} = F_D + m_p g\left(\frac{\rho_p - \rho}{\rho_p}\right) + F \quad (13)$$

where m_p, $\vec{v}_p$, and ρ_p are, respectively, the mass, velocity, and density of the particle. The $\vec{F}_D$ is the drag force, defined as follows

$$F_D = \frac{1}{2}\rho C_d A_p |v - v_p|(v - v_p) \quad (14)$$

where A_p is the cross-sectional area of the particle and C_d is the drag force coefficient, calculated as the spherical drag law proposed by Morsi and Alexander.[56] $\vec{F}$ includes the so-called virtual mass, $\vec{F}_{VM}$, and the pressure gradient force, $\vec{F}_{PG}$.

$$F_{VM} = \frac{1}{2}m_p \frac{\rho}{\rho_p}\left(\frac{Dv}{Dt} - \frac{dv_p}{dt}\right) \quad (15)$$

$$F_{PG} = m_p \frac{\rho}{\rho_p}\frac{Dv}{Dt} \quad (16)$$

where D/Dt is the material derivative.

3.2. Grid Sensitivity Analysis. A uniform structured hexahedral mesh is created and a sensitivity analysis is carried out to ensure that the numerical calculation results are not affected by the grid density and time step. The simulation runs for several oscillation periods until the difference between the results from one oscillation period to the next is negligible, and the result is considered stable. Table 2 summarizes the

Table 2. Results of Grid Sensitivity Analysis

mesh	elements (reactor cell) (k)	vorticity magnitude (%)
1	110	24.8
2	150	25.1
3	190	0.7
4	280	0.5
5	340	

dimensions of the five meshes employed for the analysis. The volume-averaged vorticity magnitude is tested for meshes #1, #2, #3, #4, and the relative error with respect to the solution in mesh #5 is computed according to

$$\text{error}\ (\%) = \left|\frac{\varnothing_i - \varnothing_5}{\varnothing_5}\right| \times 100, \quad i = 1, 2, 3, 4. \quad (17)$$

where $\varnothing$ is the physical quantity evaluated, which represents the vorticity magnitude in the paper.

Configuration #3 is selected since it shows the better relation between computational cost and the accuracy of the results.

3.3. Numerical Method and Boundary Conditions. The pressure-based solver is used. The least squares cell-based gradient method is selected, with the second-order scheme used for pressure and momentum.[57] Finally, the SIMPLE pressure−velocity coupling scheme and second-order implicit for the transient formulation have been used.

In oscillatory flow conditions, the inlet velocity (eq 18) with a net flow rate and a superimposed periodic oscillation is adopted to ensure that the volume of periodic oscillation is constant under different oscillation frequencies. The inlet temperature of the solution is 313.15 K. For the cooling crystallization process, the wall temperature is set at 303.15 K. The inner surface of the tube wall is prescribed nonslip, and the constant gauge static pressure of 0 Pa is prescribed at the tube outlet. To minimize the effect of boundary conditions on the main flow, the first two and the last baffle cells are discarded in the calculation of fluid information. Paracetamol solution (ρ = 976.1 kg·m^{-3}, μ = 0.00108 kg·m^{-1}·s^{-1}) is the selected fluid for this study. Paracetamol granules (ρ_p = 1263 kg·m^{-3}, particle diameter: 95 μm) are selected as seeds with a volume fraction below 10%. Monosized spherical particles are modeled for the purpose of simplicity. The net flow rate is 0.005 m·s^{-1}

$$u = 2\pi f x_0 \sin(2\pi f t) + u_{net} \quad (18)$$

4. RESULTS AND DISCUSSION

4.1. Effect of Re_o on the MSZW. The evolution trend of the MSZW changing with the Re_o is shown in Figure 3, in

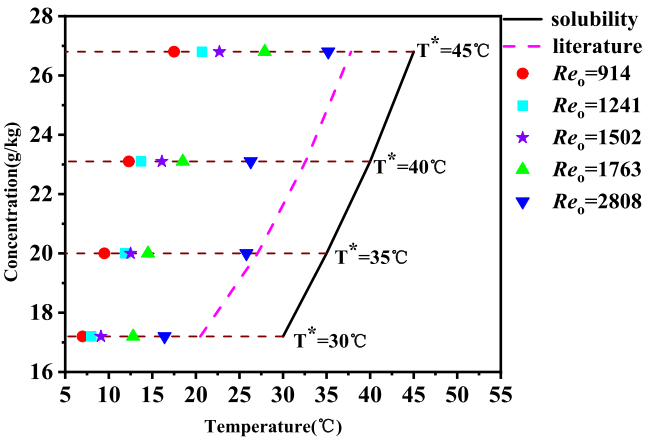

Figure 3. Variation of the MSZW with Re_o at the cooling rate 30 ° C·h^{-1} (MSZW is the difference between the saturation temperature of the solution and the detected temperature of the crystal).

which the solid black line indicates the solubility curve. From Figure 3, it can be seen that the crystallization temperature of the solution gradually increases with an increase in Re_o, resulting in a narrower MSZW. Such a result is in accordance with the previous research on the agitation system.[41,58] From Figure 3, it can be carried out that the Re_o decreases from 2808 to 914, and the MSZW increases by 123%. Moreover, Table 3 shows that the average MSZW in the OFC is about three times of that in the stirring system[44] when it is provided with the similar power densities (OFC-1.9 Hz, 370 w·m^{-3} and STR-350 rpm, 340 w·m^{-3} data from literature[49]), indicating that the OFC system has a more stable crystallization environment than the stirring system, which can provide a wider operating

https://doi.org/10.1021/acsomega.1c03890
ACS Omega 2021, 6, 28912−28922

Table 3. Power Density (P/V) for the OFC at the Cooling Rate 30 °C·h^{-1}

type of crystallizer and operating conditions	P/V (w·m^{-3})	average MSZW (°C)
OFC, 1.4 Hz (Re_o = 914)	148	25.9
OFC, 1.9 Hz (Re_o = 1241)	370	23.9
OFC, 2.3 Hz (Re_o = 1502)	843	22.3
OFC, 2.7 Hz (Re_o = 1763)	1062	19.0
OFC, 4.3 Hz (Re_o = 2808)	4292	11.6
STR, 350 rpm	340	8

window for the crystallization process. Even though the power density is increased by 11 times, the MSZW is still larger than that of the stirring system. It is not difficult to infer that the system with a wider metastable zone means a large supersaturation is required for nucleation. Therefore, the process of nucleation for a given crystallization system can be easily controlled in the OFC.[12]

4.2. Effect of Cooling Rate on the MSZW and Determination of Nucleation Kinetic Parameters. Figure 4a shows the effects of different cooling rates (β) on the MSZW when Re_o is chosen 1763. The overall effect is that the faster the cooling rate, the wider the MSZW becomes, which is similar to the previous literature.[39,41,47] This is attributed to that a faster cooling rate usually leads to a faster increase in supersaturation. Coupling with a delayed nucleation response, the nucleation rate cannot keep up with the concentration gradient, and the MSZW consequently becomes larger. Compared with the STR system in the previous literature,[44] the OFC system has a wider metastable zone at a similar cooling rate, for example, 30 or 5 °C·h^{-1}, as shown in Figure 4a.

Except for the MSZW, it is also necessary to test whether the nucleation kinetic characteristics in the OFC system are similar or at the same level as the STR system. In this work, experimental data at a saturation temperature of 30 °C are adopted to plot the relationship between the cooling rate and MSZW according to eq 9. The nucleation kinetic parameters are obtained by linear regression (R^2 = 0.97), as shown in Figure 4b. Table 4 compares the nucleation order n and the mass nucleation rate constant k_n in the OFC system with those in the STR.[41] The results show that the nucleation rate of an OFC is close to that of an STR in a certain operating range,

Table 4. Evaluation of Nucleation Kinetic Parameters

type of crystallizer	n	k_n(kg·m^{-3}·min^{-1})
OFC	1.89	0.240
STR	1.68	0.206

which indicates that the OFC has similar nucleation capability and that the increase of MSZW is not at the expense of the nucleation rate.

4.3. Operating Advantages Provided by the Flow Characteristics of OFC. *4.3.1. Distribution and Evolution Characteristics of Vortex and Shear Strain Rate (SSR) Inside the OFC.* To demonstrate the operational advantages and clarify the mechanism underlying the continuous crystallization process in the OFC, the detailed flow characteristics inside the OFC are investigated numerically. The two-dimensional velocity distribution inside a middle cavity of the OFC in a typical oscillatory period is illustrated when Re_o is chosen to be 914 in Figure 5a. According to the characteristics of the sine curve, the oscillation process of a single period can be divided into six stages. Initially, at the moment of t/τ = 0.18 in the oscillation cycle, the axial velocity is the highest at the contraction of the tube, and eddies form at the bottom of the tube. Then, at the moment of t/τ = 0.28, the regions of higher velocity become stretched in the axial direction, and vortexes begin to strengthen and extend, exceeding half a cavity length. Next, at the moment of flow reversal (t/τ = 0.5), the vortex began to detach from the baffle edge, which also reduces the intensity of the core flow. Similar characteristics of vortex distribution occur in the next half of the oscillation cycle. Those results also show that the generation of vortices is nonaxisymmetric and the flow becomes chaotic, especially at the moment of flow reversal (t/τ = 0.5 and 0.98). Distributions of vorticity and SSR are also demonstrated in Figure 5b,c, and it reveals that their developments are highly matched with the vortex region in the velocity field. This result first proves that the OFC can produce periodic disturbance to the flow field and avoid the long stay of fluid in a fixed position, thus preventing the formation of persistent and strong disturbance locally.

Then, the evolution of the local vortex intensity is analyzed in detail. Figure 6a shows the instantaneous distribution of the mean vortex intensity on the $X-Z$ cross sections along the Y direction. It can be seen that the vortex intensity is periodically

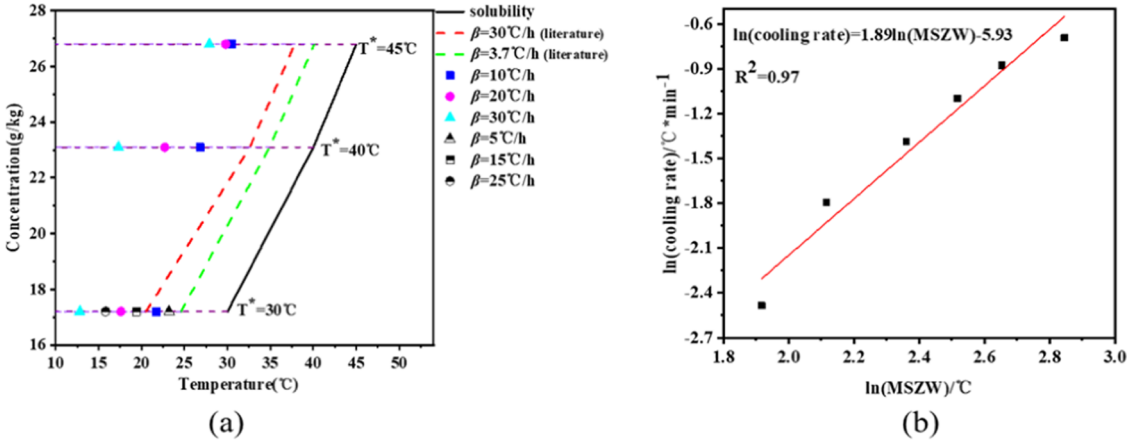

Figure 4. (a) Relationship between the cooling rate and MSZW (data of red and green dashes are from ref 43). (b) Apparent nucleation orders estimated from the MSZW data for a saturation temperature of 30 °C.

https://doi.org/10.1021/acsomega.1c03890
ACS Omega 2021, 6, 28912−28922

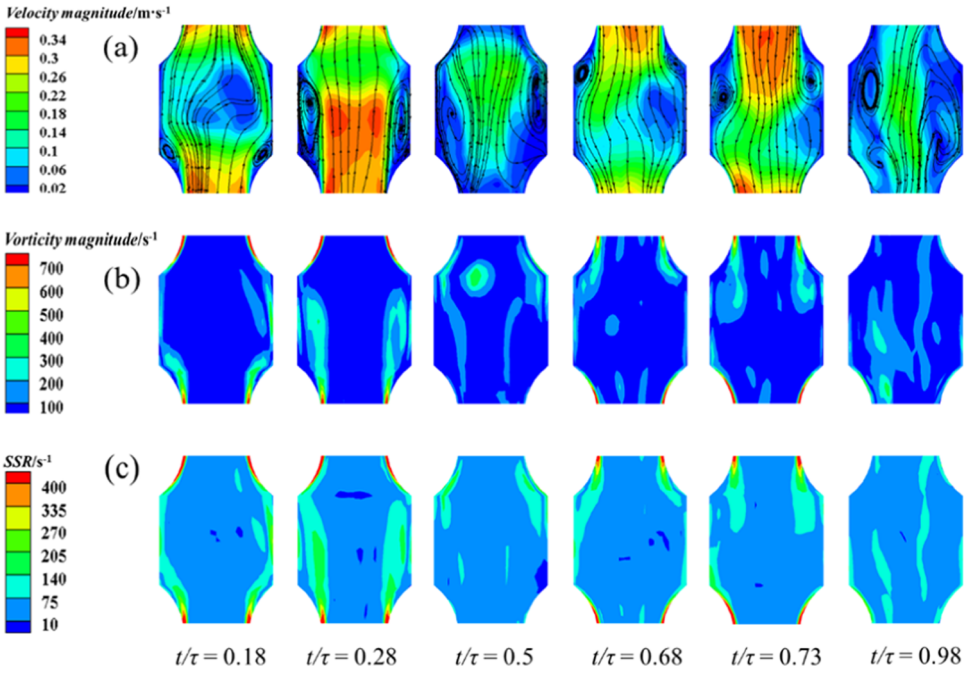

Figure 5. Contours of velocity vector (top-a), vorticity magnitude (middle-b), and SSR field (bottom-c) at different times in the $X-Y$ plane under Re_o = 914.

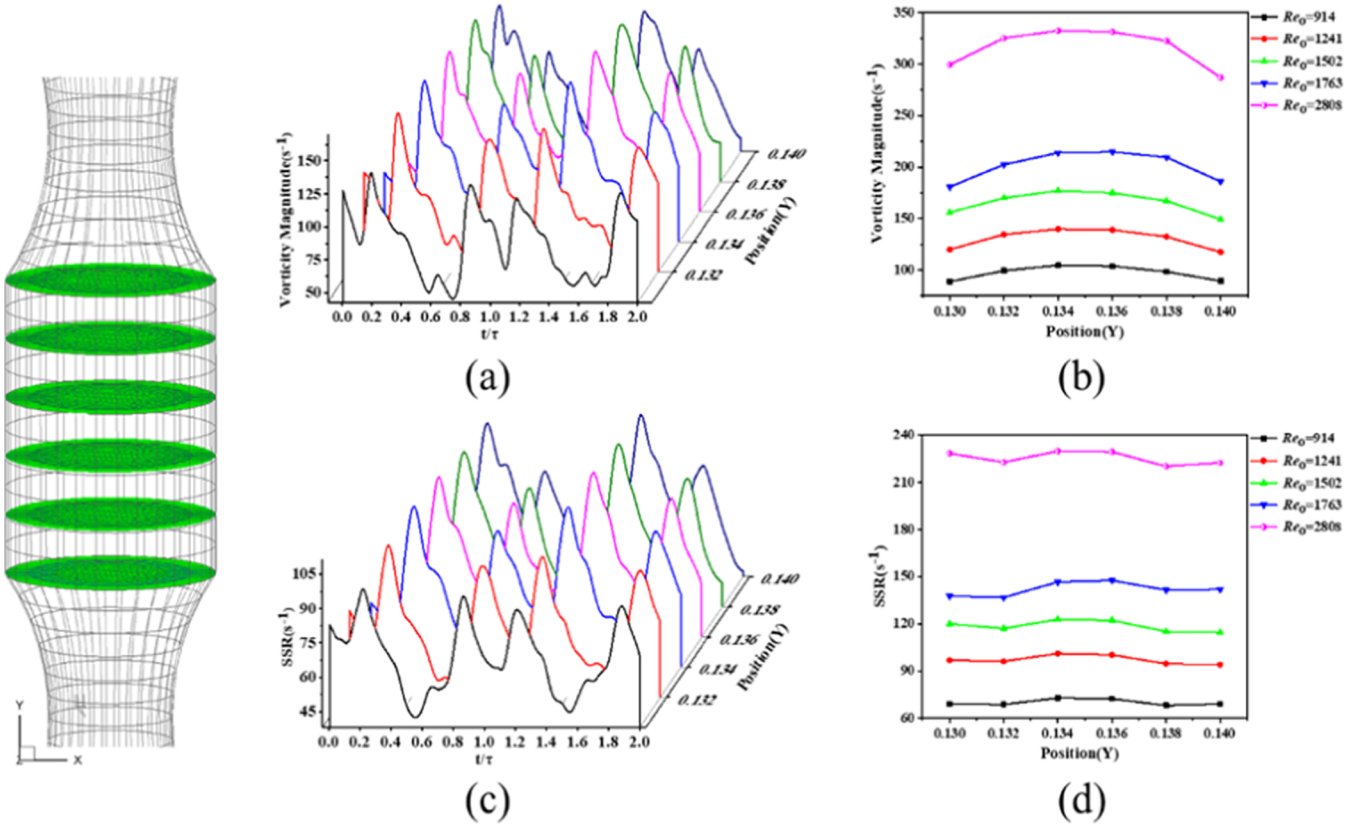

Figure 6. Instantaneous distribution of the (a) vortex intensity and (c) SSR with different cross sections along the Y direction (Re_o = 914); time-averaged distribution of the (b) vortex intensity and (d) SSR with different cross sections along the Y direction under different Re_o.

distributed on the same section, while the vortex intensity is periodically distributed along the Y direction with time. According to classical nucleation theories, the mechanism of secondary nucleation includes contact nucleation (particle−impeller, particle−particle, and particle−wall) and fluid shear nucleation. Because the OFC can avoid stirring, the driving force of the particle−particle and particle−wall collision is provided by the flow field in the OFC alone. Therefore, the local instantaneous strong vortex disturbance in the OFC is conducive to secondary nucleation. Simultaneously, the vortex

https://doi.org/10.1021/acsomega.1c03890
ACS Omega 2021, 6, 28912−28922

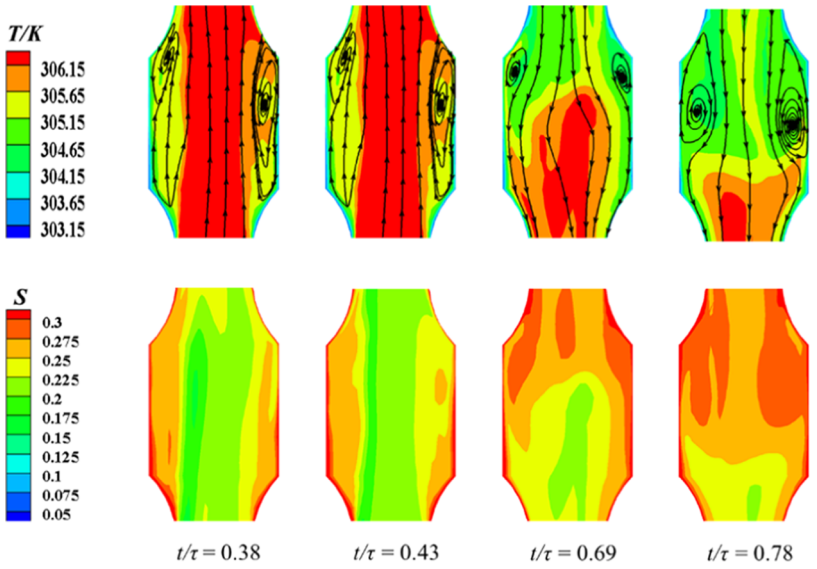

Figure 7. Temperature and relative supersaturation fields on the $X-Y$ plane (Re_o = 914, Z = 0).

which circulates along a specific route in the internal space periodically can avoid the persistence of the strong disturbance at a fixed position. Furthermore, combined with the statistical data about the time-averaged distribution of the vortex intensity shown in Figure 6b, it can be seen that the average vortex intensity is relatively stable and weak in space, indicating that the overall crystallization environment provided by the OFC is stable and moderate, which is beneficial to the growth of the crystal nucleus and the maintenance of the operation window.

The above analysis about the influence of the flow field on contact nucleation is based on the concept of the vortex intensity. At the same time, fluid shear nucleation, another mechanism of secondary nucleation, also plays a crucial role in nucleation.[59,60] Therefore, it is necessary to further analyze the evolution characteristics of the shear flow in the OFC. The shear flow is caused by periodic oscillation, which can be characterized by the SSR. The instantaneous distribution of the SSR on the X-Z cross section along the Y direction and the time-averaged distribution of the SSR under different Re_o are shown in Figure 6c,d. The result shows that the distribution characteristics of SSR are similar to those of the vortex intensity. The instantaneously strong SSR is conducive to shear nucleation, whereas a periodical circulation of strong SSR indicates the shifting of intensive shear nucleation sites. The average SSR also indicates that the OFC system is moderate and stable, which is conducive to the growth of the crystal nucleus and the maintenance of the operation window.

Based on the above analysis, the OFC can produce both moderate and disturbed crystallization environments, which reveals the internal mechanism of OFC. The locally instantaneously strong vortex disturbance and SSR are conducive to the secondary nucleation. As the vortex is generated along a specific route, the formation of a persistent strong disturbance at fixed positions is avoided. Meanwhile, the time-averaged vortex intensity and SSR are uniform and even at a low level, which can supply a moderate environment for the growth of the crystal nucleus and the maintenance of the operation window.

4.3.2. Temperature and Supersaturation Field Evolution. For the cooling crystallization process, in addition to the influence of the flow field, the heat transfer characteristics of the flow process, as well as the evolution of the temperature and relative supersaturation (S) field should also be investigated. Figure 7 shows the temperature and relative supersaturation changes during a cycle under Re_o = 914. The temperature declination first occurs at the location, where the vortex appears and evolves according to the vortex flow field. The relative supersaturation presents the opposite trend, which is relatively higher at the location, where the vortex appears. It shows that the heat transfer enhancement area in the OFC is coupled with the vortex and shear enhancement area.

4.3.3. Stirring Effect without Impeller in the OFC. The spatially averaged values of the SSR in the OFC under different Re_o are obtained by numerical simulation results, as shown in Table 5. Among them, STR-600 and STR-800 are the SSRs of the paracetamol aqueous solution on the crystallization experiment in the stirring system.[31] It can be found that the OFC provides higher SSR and promote crystallization nucleation. However, it can be inferred that $MSZW_{STR\text{-}350}$ > $MSZW_{STR\text{-}600}$ > $MSZW_{STR\text{-}800}$ taking the changing rule of the metastable zone in Figure 3 into consideration, which proves that the OFC provides a wider metastable zone. This implies that the nucleation of the STR-600 and STR-800 systems is mainly caused by mechanical stirring.

Table 5. SSR under Different Operating Conditions during Crystallization

type of crystallizer	operating conditions	volume-averaged SSR (s^{-1})
OFC	1.4 Hz	77
OFC	1.9 Hz	107
OFC	2.3 Hz	132
OFC	2.7 Hz	157
OFC	4.3 Hz	254
STR	600 rpm	18
STR	800 rpm	20

The results of McGlone[8] showed that volume-averaged shear rates of OFRs are an order of magnitude larger than those of an STR. Although it may be satisfactory to consider the average SSR when correlating power, velocity, and other

https://doi.org/10.1021/acsomega.1c03890
ACS Omega 2021, 6, 28912−28922

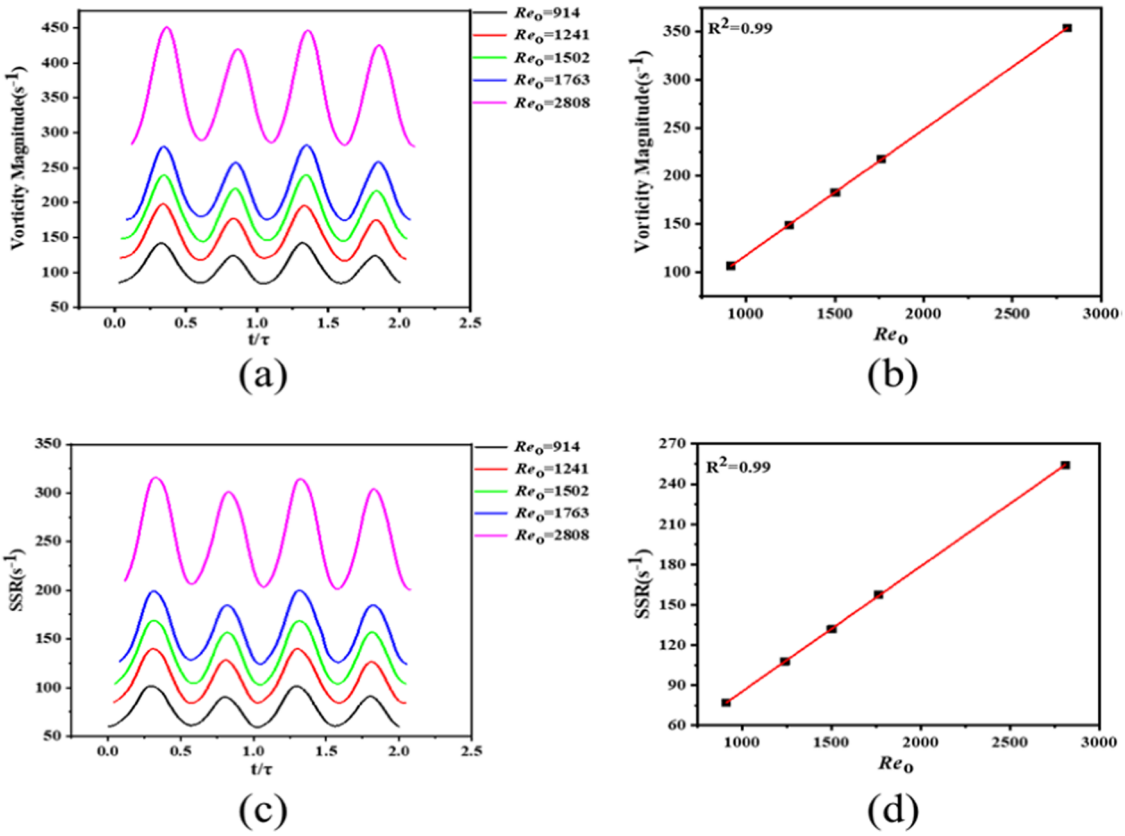

Figure 8. Instantaneous distribution of the (a) volume-averaged vortex intensity and (c) SSR at different Re_o; the time-averaged value of the (b) volume vortex intensity and (d) SSR varies with the Re_o.

data in fluid mixing applications, it is not the case in some applications involving the deformation and breaks of bubbles, granular aggregates, and biological cells, where the maximum shear rate needs to be considered. At the same time, Wu[61] found that the maximum SSR is obviously localized on the impeller blade surface, which is several orders of magnitude higher than the average SSR. Therefore, unlike STR, OFC avoids the high shear characteristic near the impeller, providing a relatively stable environment for the crystallization process. It can also be indicated that the OFC suppresses the premature occurrence of spontaneous nucleation and increases the MSZW.

4.4. Optimal Operating Parameters of OFC. For a specific size of the OFC with smooth periodic constrictions, the Re_o is particularly crucial for the crystallization process. Figure 8a shows the instantaneous distribution of the volume-averaged vortex intensity at different Re_o in any two periods. It can be found that the vortex intensity changes periodically with time. At the same time, it can be seen from Figure 8b that the time-averaged vortex intensity is linearly related to the Re_o. With the increase of Re_o, the vortex intensity of the fluid increases, which is conducive to the formation of secondary nucleation.

Simultaneously, the influence of Re_o on the SSR is investigated in Figure 8c. The SSR of the whole crystallization system increases with the increase of Re_o and changes periodically, which are similar to those of the vortex intensity. Figure 8d shows the time-averaged SSR is linearly related to the Re_o, which further indicates that the increase of the SSR is beneficial to the flow shear nucleation.

Finally, based on the experimental and numerical simulation analysis of the OFC, the increase of Re_o is conducive to secondary nucleation, but the MSZW becomes narrow, and the operating window of the crystallization process will be limited. Therefore, it should be an optimization interval for the Re_o to balance the MSZW and the secondary nucleation rate, thus optimizing the crystallization process. As shown in Figure 9, when the saturation temperature is 30 °C and the cooling rate is 30 °C·h^{-1}, the optimal operation range for Re_o is 1862−1881.

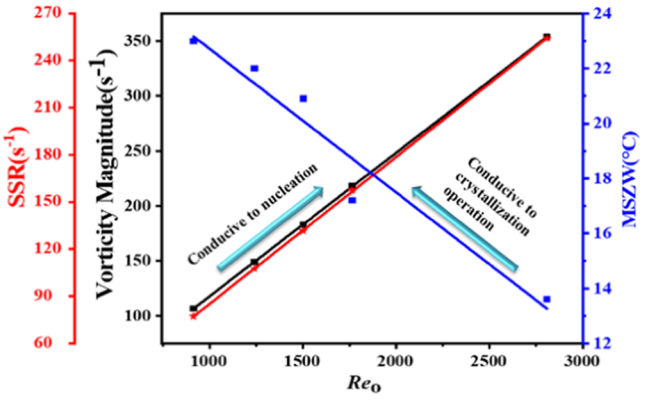

Figure 9. Operation parameter optimization of the OFC (T^* = 30 °C).

https://doi.org/10.1021/acsomega.1c03890
ACS Omega 2021, 6, 28912−28922

5. CONCLUSIONS

The cooling crystallization process of the paracetamol−water solution is studied using the OFC with smooth periodic contractions, and the dual effects of oscillatory flow on the MSZW and the secondary nucleation rate are investigated.

From the experimental results, the MSZW decreases with the increase of Re_o and increases with the increase of the cooling rate in the OFC. The Re_o falls from 2808 to 914, and the increment of MSZW is 123%. Moreover, at the same power density, the MSZW of the OFC is about three times that of the conventional STR. Even though the power density is increased by 11 times, the MSZW is still larger than that of the stirring system, indicating that the OFC can provide a wider operating window and a relatively stable environment for the crystallization process.

Combined with the numerical simulation analysis, the local instantaneous strong vortex intensity and SSR in the OFC are conducive to the secondary nucleation. Moreover, the vortex generated by the oscillatory flow circulates through the internal space periodically along a certain route, avoiding the formation of a persistent strong disturbance at a fixed position. Meanwhile, the time-averaged vortex intensity and SSR are uniform and even at a low level in space, indicating that the overall crystallization environment provided by the OFC is stable and moderate, which is beneficial to the growth of the crystal nucleus and the maintenance of the operation window. For the cooling crystallization process, the temperature and supersaturation fields evolve in accordance with the evolution of the vortex.

Above all, the increase of Re_o will promote the secondary nucleation and decrease the MSZW. Therefore, the appropriate operating conditions should be selected by balancing the nucleation rate and the crystallization operation window. Under the process conditions of this study, the optimal operation range for Re_o is 1862−1881. Since the scale-up of the OFC can be linearly treated, the optimization parameter should be valuable for the industrial crystallization process.

AUTHOR INFORMATION

Corresponding Author

Zhong Lan − *Liaoning Key Laboratory of Clean Utilization of Chemical Resources, Institute of Chemical Engineering, Dalian University of Technology, Dalian 116024, China;* orcid.org/0000-0001-5621-4532; Phone: +86 189 4095 3235; Email: lanzhong@dlut.edu.cn

Authors

Shi-jun Lian − *Liaoning Key Laboratory of Clean Utilization of Chemical Resources, Institute of Chemical Engineering, Dalian University of Technology, Dalian 116024, China*

Zhong-xin Hu − *Liaoning Key Laboratory of Clean Utilization of Chemical Resources, Institute of Chemical Engineering, Dalian University of Technology, Dalian 116024, China*

Rong-fu Wen − *Liaoning Key Laboratory of Clean Utilization of Chemical Resources, Institute of Chemical Engineering, Dalian University of Technology, Dalian 116024, China*

Xue-hu Ma − *Liaoning Key Laboratory of Clean Utilization of Chemical Resources, Institute of Chemical Engineering, Dalian University of Technology, Dalian 116024, China*

Complete contact information is available at: https://pubs.acs.org/10.1021/acsomega.1c03890

Notes

The authors declare no competing financial interest.

ACKNOWLEDGMENTS

This work was financially supported by the National Natural Science Foundation of China (No. 51836002).

NOMENCLATURE

API	active pharmaceutical ingredient
ATR-FTIR	attenuated total reflection Fourier transform infrared spectroscopy
FBRM	focused beam reflectance measurements
MSZW	metastable zone width
OFC	oscillatory flow crystallizer
OFR	oscillatory flow reactor
PVM	particle vision and measurement
SSR	shear strain rate
STR	stirred tank reactor
A	reactor's cross-sectional area, m^2
A_p	cross-sectional area of a particle, m^2
C	concentration, $g{\cdot}kg^{-1}$
C^*	solubility concentration, $g{\cdot}kg^{-1}$
ΔC	supersaturation, $g{\cdot}kg^{-1}$
C_D	discharge coefficient of the baffles
C_d	drag force coefficient
C_P	fluid specific heat, $J{\cdot}Kg^{-1}{\cdot}K^{-1}$
d	tube inner diameter, m
F	force, N
f	oscillation frequency, Hz
F_D	drag force, N
F_{VM}	virtual mass force
F_{PG}	pressure gradient force
g	gravity, $m{\cdot}s^{-2}$
h	volume shape factor
J_m	mass nucleation rate, $kg/min^{-1}{\cdot}m^{-3}$
J_n	nucleation rate, $\#/min^{-1}{\cdot}m^{-3}$
k	thermal conductivity, $W{\cdot}m^{-1}{\cdot}K^{-1}$
k_n'	number nucleation rate constant
k_n	mass nucleation rate constant
m_p	particle mass, kg
n_o	number of orifices
P	pressure, Pa
P/V	power density, $w{\cdot}m^{-3}$
Re_o	oscillation Reynolds number
r	critical nucleus size, m^{-1}
S	relative supersaturation, $S=(C - C^*)/C^*$
St	Strouhal number
T	temperature, K
t	time, s
u_{net}	net flow rate, $m{\cdot}s^{-1}$
V	reactor's volume, m^3
$\vec{v}$	velocity vector, $m{\cdot}s^{-1}$
v_p	particle velocity vector, $m{\cdot}s^{-1}$
x_o	amplitude, m
α	the ratio of the area of orifice over the area of the tube (the restriction ratio)
β	cooling rate, $°C{\cdot}h^{-1}$
ρ	fluid density, $kg{\cdot}m^{-3}$
ρ_p	particle density, $kg{\cdot}m^{-3}$
μ	fluid viscosity, $kg{\cdot}m^{-1}{\cdot}s^{-1}$
τ	oscillation period, s^{-1}
ε	conversion factor
$\varnothing_i$	physical quantity

https://doi.org/10.1021/acsomega.1c03890
ACS Omega 2021, 6, 28912−28922

REFERENCES

(1) Mangin, D.; Garcia, E.; Gerard, S.; Hoff, C.; Klein, J.; Veesler, S. Modeling of the dissolution of a pharmaceutical compound. *J. Cryst. Growth* **2006**, *286*, 121−125.

(2) Olesberg, J.; Arnold, M.; Hu, S.-Y. B.; Wiencek, J. M. Temperature-insensitive near-infrared method for determination of protein concentration during protein crystal growth. *Anal. Chem.* **2000**, *72*, 4985−4990.

(3) Shi, D.; Mhaskar, P.; El-Farra, N. H.; Christofides, P. D. Predictive control of crystal size distribution in protein crystallization. *Nanotechnology* **2005**, *16*, S562−S574.

(4) Aamir, E.; Nagy, Z. K.; Rielly, C. D. Optimal seed recipe design for crystal size distribution control for batch cooling crystallisation processes. *Chem. Eng. Sci.* **2010**, *65*, 3602−3614.

(5) Zhang, D.; Xu, S.; Du, S.; Wang, J.; Gong, J. Progress of pharmaceutical continuous crystallization. *Engineering* **2017**, *3*, 354−364.

(6) Gao, Z.; Rohani, S.; Gong, J.; Wang, J. Recent developments in the crystallization process: toward the pharmaceutical industry. *Engineering* **2017**, *3*, 343−353.

(7) Variankaval, N.; Cote, A. S.; Doherty, M. F. From form to function: Crystallization of active pharmaceutical ingredients. *AlChE J.* **2008**, *54*, 1682−1688.

(8) Mcglone, T.; Briggs, N. E. B.; Clark, C. A.; Brown, C. J.; Sefcik, J.; Florence, A. J. Oscillatory Flow Reactors (OFRs) for Continuous Manufacturing and Crystallization. *Org. Process Res. Dev.* **2015**, *19*, 1186−1202.

(9) Vedantam, S.; Ranade, V. V. Crystallization: Key thermodynamic, kinetic and hydrodynamic aspects. *Sadhana* **2013**, *38*, 1287−1337.

(10) Botsaris, G. D. Secondary Nucleation—A Review. In *Industrial Crystallization*; Plenum Press, 1976; pp 3−22.

(11) Pandit, A. V.; Ranade, V. V. Fluidic Oscillator as a Continuous Crystallizer: Feasibility Evaluation. *Ind. Eng. Chem. Res.* **2020**, *59*, 3996−4006.

(12) Yousuf, M.; Frawley, P. J. Experimental Evaluation of Fluid Shear Stress Impact on Secondary Nucleation in a Solution Crystallization of Paracetamol. *Cryst. Growth Des.* **2018**, *18*, 6843−6852.

(13) Chen, J.; Sarma, B.; Evans, J. M. B.; Myerson, A. S. Pharmaceutical Crystallization. *Cryst. Growth Des.* **2011**, *11*, 887−895.

(14) Plumb, K. Continuous Processing in the Pharmaceutical Industry: Changing the Mind Set. *Chem. Eng. Res. Des.* **2005**, *83*, 730−738.

(15) Abbott, M.; Harvey, A.; Perez, G. V.; Theodorou, M. Biological processing in oscillatory baffled reactors: operation, advantages and potential. *Interface focus* **2013**, *3*, No. 20120036.

(16) Mackley, M. Process innovation using oscillatory flow within baffled tubes. *Chem. Eng. Res. Des.* **1991**, *69*, 197−199.

(17) Ni, X.; Mackley, M.; Harvey, A.; Stonestreet, P.; Baird, M.; Rao, N. R. Mixing through oscillations and pulsations—a guide to achieving process enhancements in the chemical and process industries. *Chem. Eng. Res. Des.* **2003**, *81*, 373−383.

(18) Stonestreet, P.; Harvey, A. A mixing-based design methodology for continuous oscillatory flow reactors. *Chem. Eng. Res. Des.* **2002**, *80*, 31−44.

(19) Mackley, M.; Stonestreet, P. Heat transfer and associated energy dissipation for oscillatory flow in baffled tubes. *Chem. Eng. Sci.* **1995**, *50*, 2211−2224.

(20) Mackley, M.; Tweddle, G.; Wyatt, I. Experimental heat transfer measurements for pulsatile flow in baffled tubes. *Chem. Eng. Sci.* **1990**, *45*, 1237−1242.

(21) Liu, Y. C.; Dunn, D.; Lipari, M.; Barton, A.; Firth, P.; Speed, J.; Wood, D.; Nagy, Z. K. A comparative study of continuous operation between a dynamic baffle crystallizer and a stirred tank crystallizer. *Chem. Eng. J.* **2019**, *367*, 278−294.

(22) Raval, V.; Siddique, H.; Brown, C. J.; Florence, A. J. Development and characterisation of a cascade of moving baffle oscillatory crystallisers (CMBOC). *CrystEngComm* **2020**, *22*, 2288−2296.

(23) Avila, M.; Fletcher, D. F.; Poux, M.; Xuereb, C.; Aubin, J. Mixing performance in continuous oscillatory baffled reactors. *Chem. Eng. Sci.* **2020**, *219*, No. 115600.

(24) Mazubert, A.; Fletcher, D.; Poux, M.; Aubin, J. Hydrodynamics and mixing in continuous oscillatory flow reactors—Part I: Effect of baffle geometry. *Chem. Eng. Process. Process Intensif.* **2016**, *108*, 78−92.

(25) Palma, M.; Giudici, R. Analysis of axial dispersion in an oscillatory-flow continuous reactor. *Chem. Eng. J.* **2003**, *94*, 189−198.

(26) Phan, A. N.; Harvey, A. P. Effect of geometrical parameters on fluid mixing in novel mesoscale oscillatory helical baffled designs. *Chem. Eng. J.* **2011**, *169*, 339−347.

(27) Manninen, M.; Gorshkova, E.; Immonen, K.; Ni, X. W. Evaluation of axial dispersion and mixing performance in oscillatory baffled reactors using CFD. *J. Chem. Technol. Biotechnol.* **2013**, *88*, 553−562.

(28) Briggs, N. E.; McGinty, J.; McCabe, C.; Raval, V.; Sefcik, J.; Florence, A. J. Heat Transfer and Residence Time Distribution in Plug Flow Continuous Oscillatory Baffled Crystallizers. *ACS Omega* **2021**, *6*, 18352−18363.

(29) Peña, R.; Oliva, J. A.; Burcham, C. L.; Jarmer, D. J.; Nagy, Z. K. Process Intensification through Continuous Spherical Crystallization Using an Oscillatory Flow Baffled Crystallizer. *Cryst. Growth Des.* **2017**, *17*, 4776−4784.

(30) Castro, F.; Ferreira, An.; Rocha, F.; Vicente, An.; Teixeira, J. A. n. Continuous-flow precipitation of hydroxyapatite at 37 C in a meso oscillatory flow reactor. *Ind. Eng. Chem. Res.* **2013**, *52*, 9816−9821.

(31) Chew, C. M.; Ristic, R. I.; Dennehy, R. D.; De Yoreo, J. J. Crystallization of Paracetamol under Oscillatory Flow Mixing Conditions. *Cryst. Growth Des.* **2004**, *4*, 1045−1052.

(32) Ejim, L. N.; Yerdelen, S.; McGlone, T.; Onyemelukwe, I.; Johnston, B.; Florence, A. J.; Reis, N. M. A factorial approach to understanding the effect of inner geometry of baffled meso-scale tubes on solids suspension and axial dispersion in continuous, oscillatory liquid−solid plug flows. *Chem. Eng. J.* **2017**, *308*, 669−682.

(33) Yang, H.; Yu, X.; Raval, V.; Makkawi, Y.; Florence, A. Effect of oscillatory flow on nucleation kinetics of butyl paraben. *Cryst. Growth Des.* **2016**, *16*, 875−886.

(34) Cruz, P.; Rocha, F.; Ferreira, A. Determination of the critical mixing intensity for secondary nucleation of paracetamol in an oscillatory flow crystallizer. *CrystEngComm* **2018**, *20*, 829−836.

(35) Ni, X.; Gough, P. On the discussion of the dimensionless groups governing oscillatory flow in a baffled tube. *Chem. Eng. Sci.* **1997**, *52*, 3209−3212.

(36) Mackley, M. R.; Ni, X. Mixing and dispersion in a baffled tube for steady laminar and pulsatile flow. *Chem. Eng. Sci.* **1991**, *46*, 3139−3151.

(37) Ni, X.; Brogan, G.; Struthers, A.; Bennett, D. C.; Wilson, S. F. A Systematic Study of the Effect of Geometrical Parameters on Mixing Time in Oscillatory Baffled Columns. *Chem. Eng. Res. Des.* **1998**, *76*, 635−642.

(38) Jimeno, G.; Lee, Y. C.; Ni, X.-W. On the evaluation of power density models for oscillatory baffled reactors using CFD. *Chem. Eng. Process. Process Intensif.* **2018**, *134*, 153−162.

(39) Ni, X.; Liao, A. Effects of cooling rate and solution concentration on solution crystallization of L-glutamic acid in an oscillatory baffled crystallizer. *Cryst. Growth Des.* **2008**, *8*, 2875−2881.

(40) Kadam, S. S.; Kramer, H. J.; ter Horst, J. H. Combination of a single primary nucleation event and secondary nucleation in crystallization processes. *Cryst. Growth Des.* **2011**, *11*, 1271−1277.

(41) Mitchell, N. A.; Frawley, P. J. Nucleation kinetics of paracetamol−ethanol solutions from metastable zone widths. *J. Cryst. Growth* **2010**, *312*, 2740−2746.

(42) Ni, X.; Liao, A. Effects of mixing, seeding, material of baffles and final temperature on solution crystallization of l-glutamic acid in an oscillatory baffled crystallizer. *Chem. Eng. J.* **2010**, *156*, 226−233.

https://doi.org/10.1021/acsomega.1c03890
ACS Omega 2021, 6, 28912−28922

(43) Dunuwila, D. D.; Berglund, K. A. ATR FTIR spectroscopy for in situ measurement of supersaturation. *J. Cryst. Growth* **1997**, *179*, 185−193.
(44) Fujiwara, M.; Chow, P. S.; Ma, D. L.; Braatz, R. D. Paracetamol crystallization using laser backscattering and ATR-FTIR spectroscopy: metastability, agglomeration, and control. *Cryst. Growth Des.* **2002**, *2*, 363−370.
(45) Lewiner, F.; Klein, J.; Puel, F.; Fevotte, G. On-line ATR FTIR measurement of supersaturation during solution crystallization processes. Calibration and applications on three solute/solvent systems. *Chem. Eng. Sci.* **2001**, *56*, 2069−2084.
(46) Trifkovic, M.; Sheikhzadeh, M.; Rohani, S. Determination of metastable zone width for combined anti-solvent/cooling crystallization. *J. Cryst. Growth* **2009**, *311*, 3640−3650.
(47) Barrett, P.; Glennon, B. Characterizing the metastable zone width and solubility curve using Lasentec FBRM and PVM. *Chem. Eng. Res. Des.* **2002**, *80*, 799−805.
(48) Mitchell, N. A.; Frawley, P. J.; Ó'Ciardhá, C. T. Nucleation kinetics of paracetamol−ethanol solutions from induction time experiments using Lasentec FBRM. *J. Cryst. Growth* **2011**, *321*, 91−99.
(49) Brown, C. J.; Ni, X.-W. Determination of metastable zone width, mean particle size and detectable number density using video imaging in an oscillatory baffled crystallizer. *CrystEngComm* **2012**, *14*, 2944−2949.
(50) Nývlt, J. Kinetics of nucleation in solutions. *J. Cryst. Growth* **1968**, *3*−*4*, 377−383.
(51) Mazubert, A.; Fletcher, D.; Poux, M.; Aubin, J. Hydrodynamics and mixing in continuous oscillatory flow reactors—Part II: Characterisation methods. *Chem. Eng. Process. Process Intensif.* **2016**, *102*, 102−116.
(52) González-Juárez, D.; Solano, J.; Herrero-Martín, R.; Harvey, A. Residence time distribution in multiorifice baffled tubes: A numerical study. *Chem. Eng. Res. Des.* **2017**, *118*, 259−269.
(53) Jiang, X.; Ruan, X.; Xiao, W.; Lu, D.; He, G. A novel membrane distillation response technology for nucleation detection, metastable zone width measurement and analysis. *Chem. Eng. Sci.* **2015**, *134*, 671−680.
(54) Ahmed, S. M.; Phan, A. N.; Harvey, A. P. Mass transfer enhancement as a function of oscillatory baffled reactor design. *Chem. Eng. Process. Process Intensif.* **2018**, *130*, 229−239.
(55) Jian, H.; Ni, X. A numerical study on the scale-up behaviour in oscillatory baffled columns. *Chem. Eng. Res. Des.* **2005**, *83*, 1163−1170.
(56) Morsi, S.; Alexander, A. An investigation of particle trajectories in two-phase flow systems. *J. Fluid Mech.* **1972**, *55*, 193−208.
(57) Nogueira, X.; Taylor, B. J.; Gomez, H.; Colominas, I.; Mackley, M. R. Experimental and computational modeling of oscillatory flow within a baffled tube containing periodic-tri-orifice baffle geometries. *Comput. Chem. Eng.* **2013**, *49*, 1−17.
(58) Liang, K.; White, G.; Wilkinson, D.; Ford, L. J.; Roberts, K. J.; Wood, W. M. L. Examination of the Process Scale Dependence of L-Glutamic Acid Batch Crystallized from Supersaturated Aqueous Solutions in Relation to Reactor Hydrodynamics. *Ind. Eng. Chem. Res.* **2004**, *43*, 1227−1234.
(59) Yousuf, M.; Frawley, P. J. Secondary Nucleation from Nuclei Breeding and Its Quantitative Link with Fluid Shear Stress in Mixing: A Potential Approach for Precise Scale-up in Industrial Crystallization. *Org. Process Res. Dev.* **2019**, *23*, 926−934.
(60) Yousuf, M.; Frawley, P. J. Quantitative Link between Secondary Nucleation and Mixing Hydrodynamics in Batch Cooling Crystallization: A New Approach in Process Development. *Org. Process Res. Dev.* **2019**, *23*, 2009−2019.
(61) Wu, J.; Graham, L. J.; Noui Mehidi, N. Estimation of agitator flow shear rate. *AIChE J.* **2006**, *52*, 2323−2332.

https://doi.org/10.1021/acsomega.1c03890
ACS Omega 2021, 6, 28912−28922